Supporting Information for

Synergistic improvement in capacitive deionization performance using a novel phase-integrated $Na_{0.55}Mn_2O_4$@$Na_{0.7}MnO_2$

Yubo Zhao [†], Yang Liu [§], Izhar Ullah Khan [†], Ao Gong [†], Silu Huo [†], Kexun Li [*,†]

[†] The College of Environmental Science and Engineering, MOE Key Laboratory of Pollution Processes and Environmental Criteria, Tianjin Key Laboratory of Environmental Remediation and Pollution Control, Nankai University, Tongyan Road No. 38, Tianjin 300071, China

[§] South-to-North Water Diversion Route Eastern Shandong Co. Ltd, Jingshidong Road No. 33399, Jinan 250109, Shandong, China

The number of pages is 11.

The number of figures is 10.

*** Corresponding author.**

E-mail addresses: likx@nankai.edu.cn (K. Li).

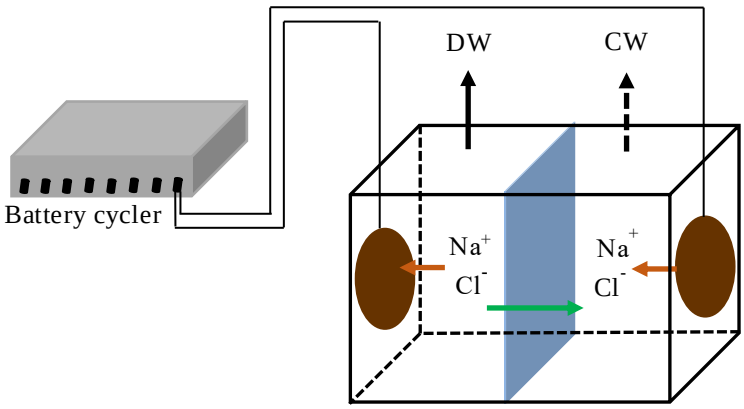

Figure S1. Schematic diagram of CDI cell. The CDI cell is comprised of a pair of symmetry NMO electrodes and an anion exchange membrane. The total volume of CDI cell is 30 mL. The distance between two electrodes was about 4 cm. The diameter of electrodess is around 3 cm and the thickness of electrodes is approximately 300 μm.

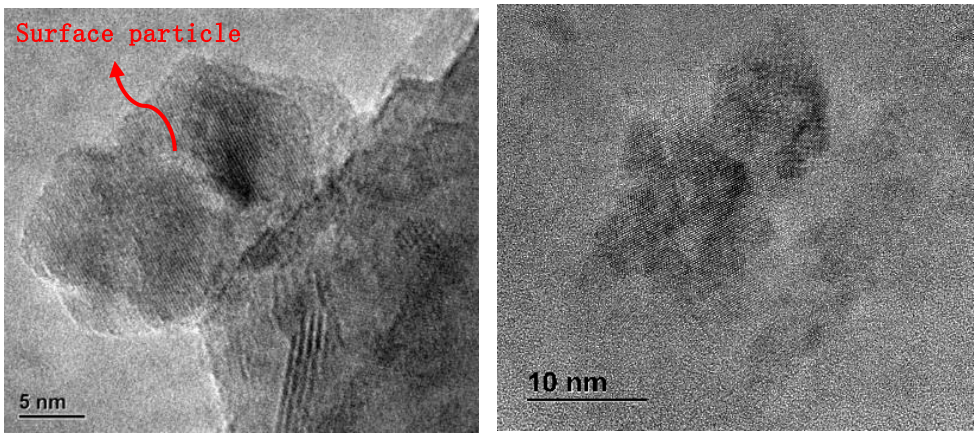

Figure S2. **High-resolution TEM images of the surface particles of NMO-800.** The adjacent lattice fringes of surface particles were 2.78 Å, corresponding to the (004) plane of $Na_{0.7}MnO_2$ phase. Therefore, the surface particles were mainly made up of $Na_{0.7}MnO_2$ phase.

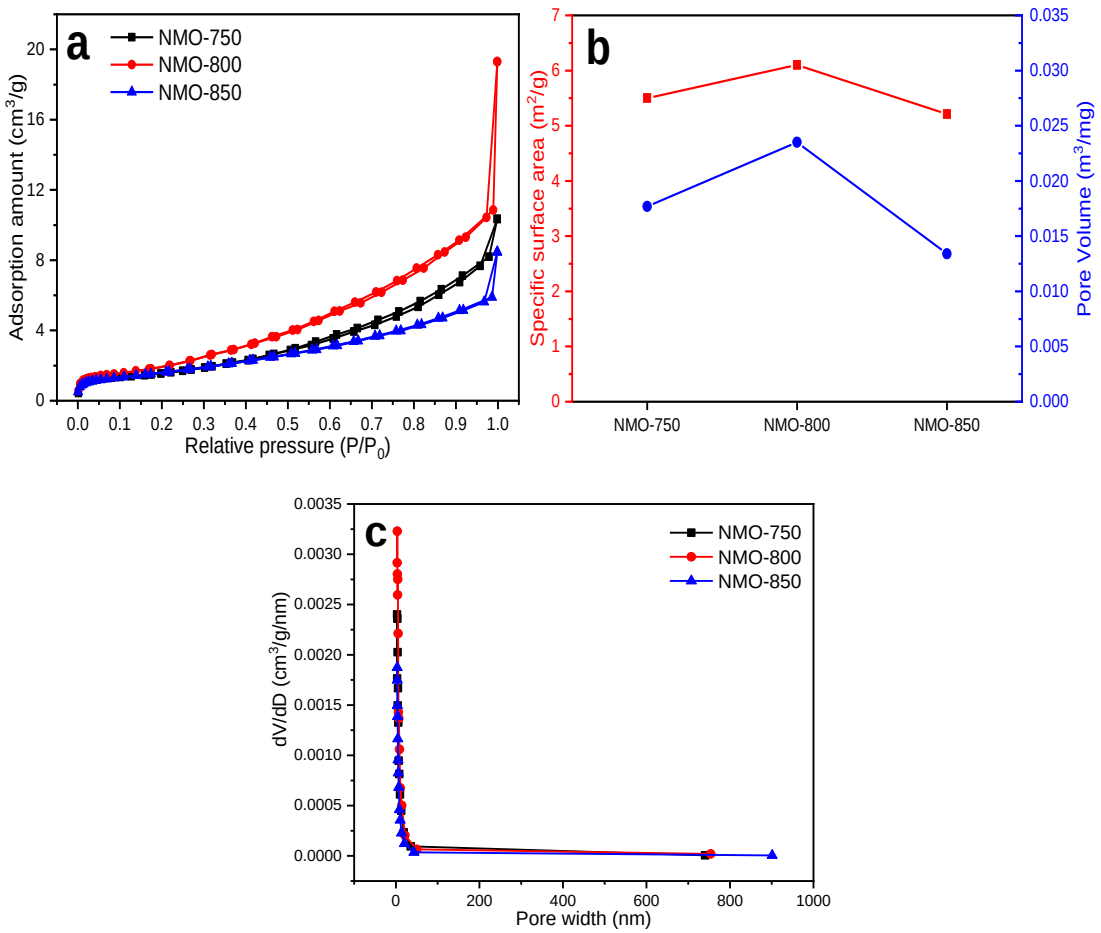

Figure S3. N_2 adsorption isotherms (a), the specific surface area and pore volume results (b), pore-size distribution curves (c) of the NMO-750, NMO-800 and NMO-850. The specific surface area and pore volume of all NMO samples were very small, demonstrating their very weak and negligible electric double layer adsorption ability for ion removal.

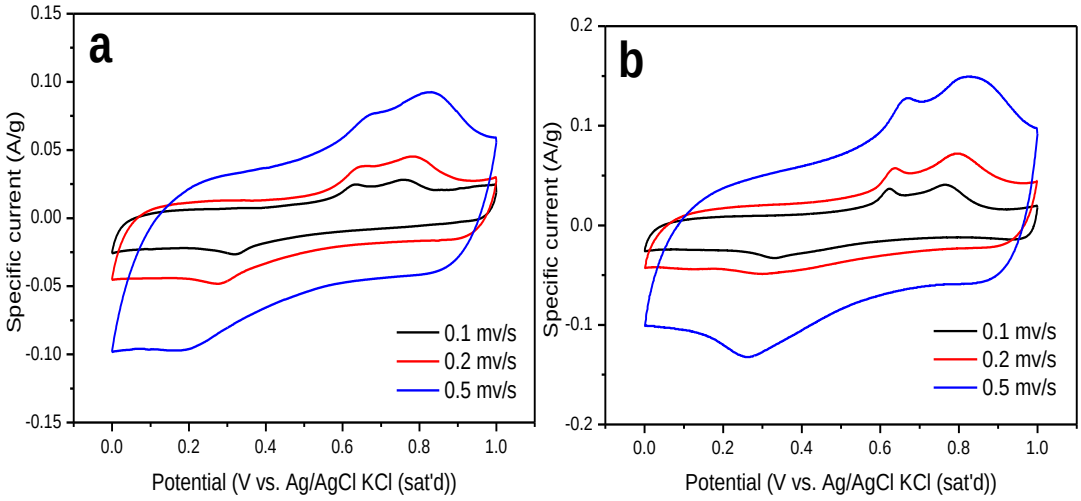

Figure S4. CV curves of the NMO-750 (a) and NMO-850 (b) with various scan rates. CV curves of both samples exhibited two distinct anodic peaks with various scan rates while only one cathodic peak possibly owing to the overlap of peaks. These observations confirmed the occurrence of deintercalation/intercalation reactions of Na ions with the NMO samples.

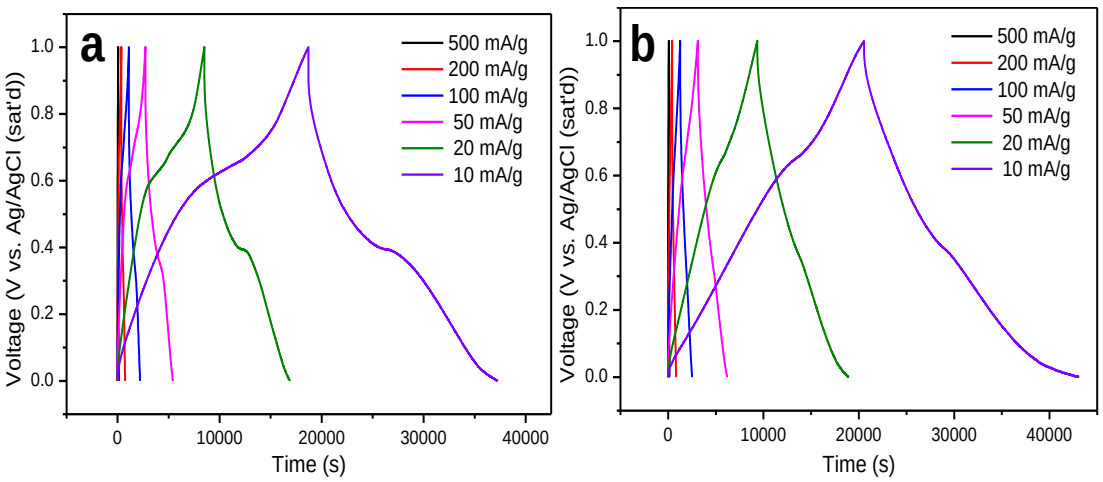

Figure S5. GCD curves of the NMO-750 (a) and NMO-850 (c) with various current densities. The nonlinear portions with the smooth slopes and charge/discharge platforms demonstrated the pseudocapacitive behavior of the NMO samples.

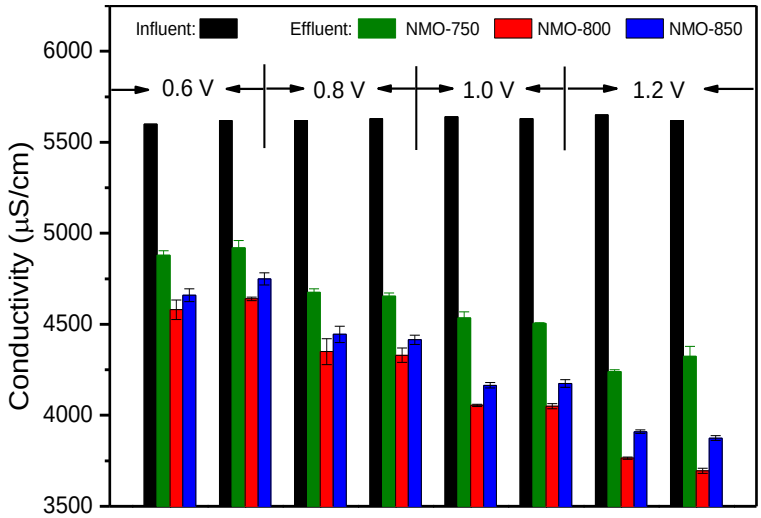

Figure S6. The conductivity data of influent and effluent of the phase-integrated NMO samples with various voltages. NMO-800 experienced higher decreases in solution conductivity than those of NMO-750 and NMO-850 with various voltages.

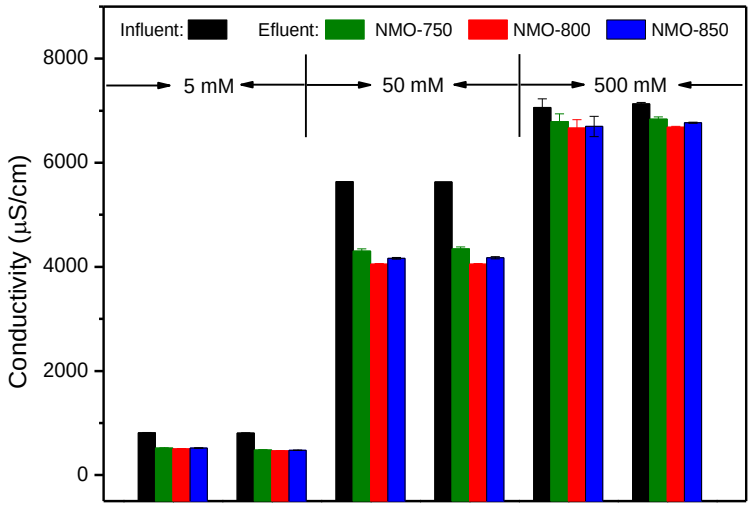

Figure S7. The conductivity data of influent and effluent of the phase-integrated NMO samples with various saline concentrations. Note: the saline solution with initial concentration of 500 mM was diluted for 10 times for the measurement of conductivity data. NMO-800 experienced higher decreases in solution conductivity than those of NMO-750 and NMO-850 with various saline concentrations.

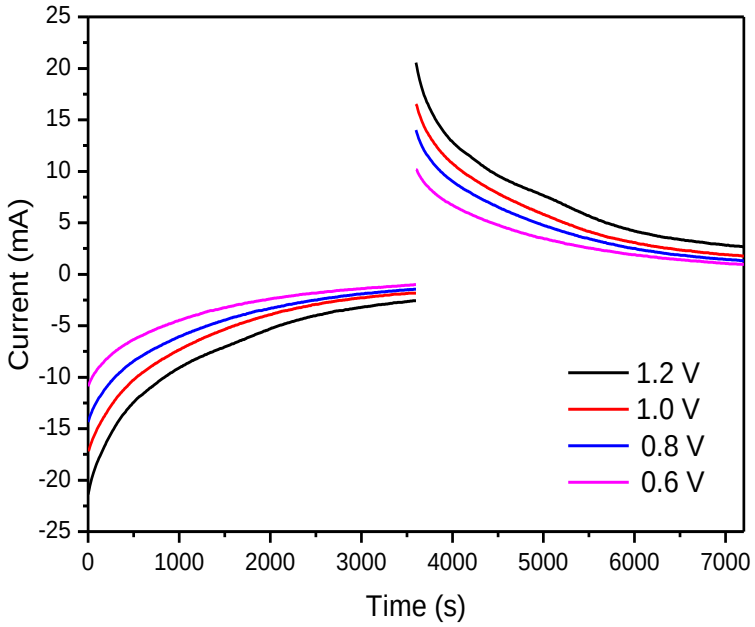

Figure S8. Time-dependent current curves of the NMO-800 with various voltages. Current profiles of NMO-800 with various voltages presented similar characteristics with the conductivity profiles, indicating that the current was mainly derived from the ions capture and release.

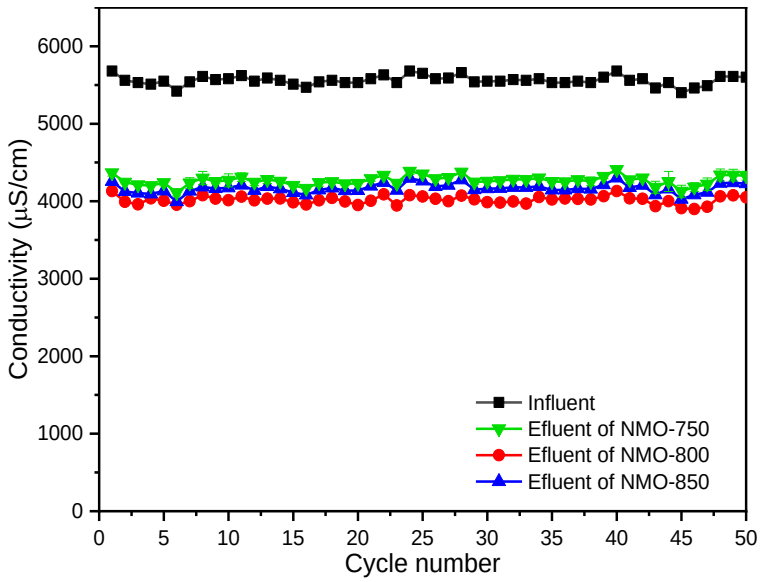

Figure S9. **The conductivity data of influent and effluent of the NMO samples over a 50-cycle period.** The change of conductivity of all NMO samples kept stable during 50 cycles.

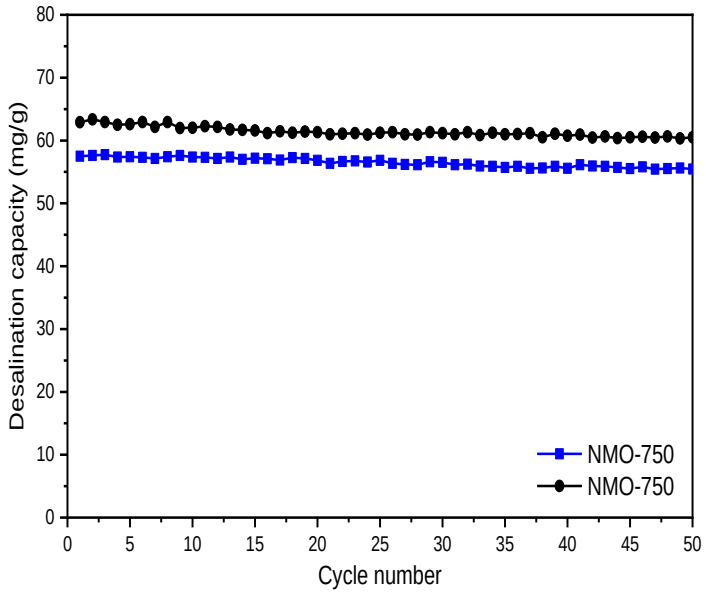

Figure S10. **Cycling stability of the NMO-750 and NMO-850 with a voltage of 1.0 V.** NMO-750 and NMO-850 displayed excellent cycling stability.